Variations on the theme of quantum optical coherence tomography: a review

**Malvin Carl Teich · Bahaa E. A. Saleh ·
Franco N. C. Wong · Jeffrey H. Shapiro**

Abstract We discuss the development of quantum optical coherence tomography (Q-OCT), an imaging modality with a number of potential applications. Although Q-OCT is not expected to replace its eminently successful classical cousin, optical coherence tomography (OCT), it does offer some advantages as a biological imaging paradigm. These include greater axial resolution and higher signal-to-background ratio, immunity to dispersion that can lead to deeper subsurface penetration, and nondestructive probing of light-sensitive samples. Q-OCT also serves as a quantum template for constructing classical systems that mimic its salutary properties.

M. C. Teich (✉)
Quantum Photonics Laboratory, Departments of Electrical & Computer Engineering,
Biomedical Engineering, and Physics, Boston University, Boston, MA, 02215, USA
e-mail: teich@bu.edu

M. C. Teich
Department of Electrical Engineering, Columbia University, New York, NY, 10027, USA

B. E. A. Saleh
Quantum Photonics Laboratory, College of Optics and Photonics (CREOL), University of Central
Florida, Orlando, FL, 32816, USA

B. E. A. Saleh
Quantum Photonics Laboratory, Department of Electrical & Computer Engineering,
Boston University, Boston, MA, 02215, USA

F. N. C. Wong
Research Laboratory of Electronics, Massachusetts Institute of Technology, Cambridge, MA,
02139, USA

J. H. Shapiro
Research Laboratory of Electronics and Department of Electrical Engineering and Computer Science,
Massachusetts Institute of Technology, Cambridge, MA, 02139, USA

1 Introduction

Time-domain optical coherence tomography (OCT) is an axial-imaging technique that makes use of classical light and classical interferometry. It utilizes a broadband optical source with short coherence length; it is therefore a form of coherence-domain imaging. The advent of nonclassical sources of light, such as twin-photon beams, has raised the question as to whether the use of such sources can serve to improve the performance of OCT. The answer turns out to be in the affirmative and a quantum version of optical coherence tomography (Q-OCT) has been developed and investigated. It does indeed offer improved imaging performance in a number of respects, but this comes at the cost of having to incorporate a source of nonclassical light in the apparatus. The development of Q-OCT has, in turn, fostered the birth of several quantum-mimetic versions of optical coherence tomography (QM-OCT) that offer the advantages of time-domain Q-OCT but make use of classical light and nonlinear optics in place of nonclassical light. The primary advantage of Q-OCT and QM-OCT over OCT is insensitivity to even-order dispersion in the medium under investigation; this can be an important consideration when dispersion sets a limit on the axial-resolution that can be achieved in conventional high-resolution OCT. In this paper, we summarize a number of theoretical and experimental studies of Q-OCT, along with its quantum-mimetic cousins (QM-OCT), in their manifold configurations.

2 OCT and its variations

2.1 Optical coherence tomography (OCT)

Optical coherence-domain reflectometry (OCDR), which was originally developed for optical-fiber and integrated-optics applications [1–3], is a high-resolution ($\sim\mu$m) axial-imaging technique that makes use of a classical broadband optical source in conjunction with a classical (second-order) interferometer [4]. When joined with transverse scanning to generate cross-sectional images, this range-finding technique has come to be called optical coherence tomography (OCT) [5]. OCT has the distinct merits that it is non-invasive, non-contact, high-resolution, and rapid. As a result, it has increasingly come to the fore as a technique that is useful for biological imaging [5–8] and clinical medicine [9, 10].

Time-domain OCT is a form of low-coherence interferometry. It makes use of the second-order coherence properties of classical light to effectively section a reflective or scattering sample with a resolution that is determined by the coherence length

of the source [11]. Sources of broad spectral width have short coherence length and therefore offer high resolution. A whole raft of optical sources have been made use of in time-domain OCT, including superluminescent diodes (SLEDs), ultrashort pulsed lasers, and supercontinuum light sources such as photonic-crystal fibers [10, chaps.2,9,10].

OCT can also be implemented in the form of frequency-domain interferometry, which offers improved detection sensitivity since echos from the entire depth of the sample are collected simultaneously, rather than sequentially. This approach offers a substantial improvement in axial-scan and data-acquisition rates because of the aforementioned increased detection sensitivity and also because mechanical scanning of the interferometer is obviated. Fourier-domain detection implementations often make use of a narrow-bandwidth optical source whose frequency is swept in time, such as a wavelength-swept laser [10, chaps.1,7,11] or a wavelength-swept amplified spontaneous emission (ASE) source [12], in conjunction with balanced detection. OCT can be carried out in various configurations, including those that are sensitive to the polarization, spectroscopic, and Doppler features of the sample [10, chaps. 21–23]; the latter can be probed by implementing OCT in a heterodyne configuration [13,14].

As the resolution of OCT has improved with the development of optical sources that generate light over broad spectral bandwidths, the deleterious effects of dispersion inherent in the sample under study have become more pronounced. In the case of ophthalmologic imaging, for example, the retinal structure of interest is located behind a comparatively large body of dispersive ocular media [15]. Sample dispersion increases the width of the coherence envelope of the probe beam and results in a reduction of axial resolution and fringe visibility [6,16,17]. To improve the resolution of OCT, it is therefore important to implement schemes for handling dispersion. Examples of techniques for depth-dependent dispersion compensation include the use of dispersion-compensating elements in the optical arrangement [15,18] and *a posteriori* numerical methods [19]. For these techniques to operate satisfactorily, however, the nature of the dispersion in the object must be well-characterized so that the appropriate optical element or numerical algorithm can be properly implemented.

2.2 Nonclassical light and quantum optical coherence tomography (Q-OCT)

Over the past several decades, a number of nonclassical (quantum) sources of light have been developed [see, for example, 20–26] and it is natural to inquire whether making use of any of these sources might be advantageous for tomographic axial imaging. An example of such a nonclassical source is spontaneous parametric down-conversion (SPDC) [27], a nonlinear optical process that generates entangled photon pairs (also called biphotons). So-called Type-I and Type-II SPDC interactions generate light with spectral/spatial and polarization entanglement, respectively [28, chap. 21]. The presence of entanglement means that photons are emitted in pairs, and are endowed with stronger-than-classical temporal and spatial correlations. By virtue of the conservation of energy and momentum in the generation process, the two photons of a pair are anti-correlated in frequencies and directions. We are indeed able to make

use of frequency-entangled twin photon pairs to construct a system that provides range measurements analogous to those obtained using classical OCT, but with a number of additional salutary nonclassical features. We refer to this scheme as quantum optical coherence tomography (Q-OCT) [29,30].

Q-OCT provides axial imaging by making use of a fourth-order interferometer that incorporates two photodetectors, rather than a second-order interferometer with a single photodetector as used for classical OCT [31]. One beam travels through the sample and the other through a controllable delay time τ (path-length delay $c\tau$) before reflection/transmission through the interferometer. The photon-coincidence rate at the output ports of the beam splitter is measured as a function of $c\tau$ by making use of a pair of photon-counting detectors and a coincidence counter. Because of quantum destructive interference, when the optical path lengths are equal, both photons emerge from the same port and the coincidence rate exhibits a sharp dip, with a width equal to that of the photon wave packet, which can be less than 10 fsec [32]. This coincidence dip is used to monitor the reflectance of the sample as a function of depth. An image of the backscattered light from a spatially extended specimen may be obtained by conducting such axial scans at a collection of transverse locations.

Entangled-photon sources, which are typically broadband marginally, have previously been used to demonstrate a number of interference effects that cannot be observed using traditional classical sources of light [see, for example, 33–35]. Twin-photon sources have also found use in quantum cryptography, metrology, ellipsometry, microscopy, and imaging [36–41], among other areas. In the context of imaging, entangled photons may be used together with photon-coincidence detectors for axial and transverse imaging, in both direct and interferometric configurations [42–44]. Some of these applications make use of the correlation properties, rather than the entanglement properties, of twin-photon sources [44].

2.3 Quantum-mimetic optical coherence tomography (QM-OCT)

Q-OCT has inspired a number of quantum-mimetic versions that operate on the basis of classical light and nonlinear optics [45–49]. Quantum-mimetic optical coherence tomography (QM-OCT) can successfully mimic dispersion cancellation and other salutary features of Q-OCT. Moreover, various versions of QM-OCT offer unique additional benefits, such as substantially increased signal-to-noise ratio and acquisition rate. The limitations of QM-OCT systems are principally associated with the complexity of the experimental arrangements though they have the distinct advantage of making use of classical light. Obviously, entanglement plays no role in QM-OCT systems.

In a similar way, quantum-mimetic transverse (ghost) imaging can also be implemented using classical light. In particular, the photon bunching associated with thermal light gives rise to photon pairs in addition to the underlying random (Poisson) photon occurrences [31,44]. A thermal source, in conjunction with a photon-coincidence or intensity-correlation measurement system, can thus mimic two-photon ghost imaging. A duality between these two imaging paradigms was formally established in 2000 [42].

3 Origin and development of quantum optical coherence tomography

3.1 Quantum optical coherence tomography (Q-OCT) theory

Figure 1a, b display schematic diagrams of time-domain OCT and Q-OCT configurations, respectively. As illustrated in Fig. 1b, Q-OCT is implemented by making use of entangled photon pairs generated in a nonlinear crystal (NLC) pumped by a laser. The reference beam, after reflection from a movable mirror, and the object beam, after reflection from an axially extended sample, impinge on the two input ports of a beam splitter. The beams that emerge from the two output ports of the beam splitter are detected by a pair of photon-counting detectors, and the coincidence rate is determined as a function of the reference-arm pathlength delay. This configuration is known as a Hong-Ou-Mandel (HOM) interferometer [32]. When the path lengths of the reference and object beams match, quantum destructive interference causes the coincidence rate to vanish. As the path length of the reference beam is varied by translating the mirror, the coincidence rate exhibits a dip at each of the reflecting boundaries within the extended sample.

In this two-photon interferometry scheme, the width of the interference dip is governed by the product $H(\Omega)H^*(-\Omega)$, where $H(\Omega)$ is the transfer function of the optical system in the object beam, and Ω is the frequency displacement from the central frequency [29,50,51]. As a result of the frequency anticorrelations in the entangled beams, the width of the dip is insensitive to even-order dispersion (including group velocity dispersion) of the imaged sample [52,53]. Methods for achieving combined even- and odd-order dispersion cancellation have also been devised [54]. As discussed above, a fundamental limitation of conventional OCT is the reduction in axial resolution that arises from sample dispersion.
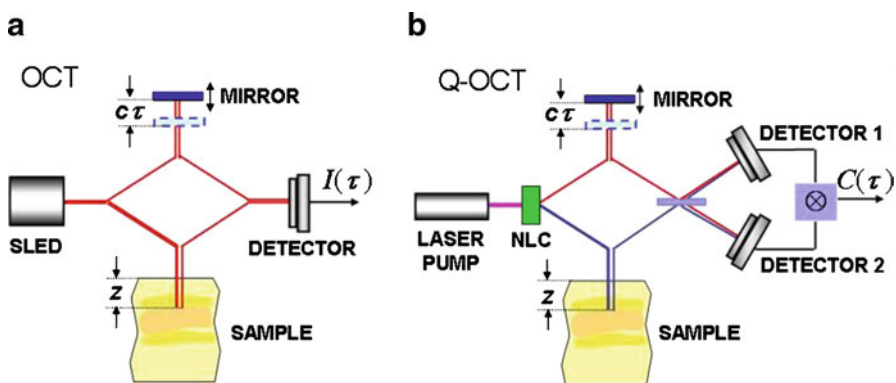

Fig. 1 **a** Conventional time-domain OCT using partially coherent light generated by a superluminescent diode (SLED) and a Michelson interferometer. The interferogram is a record of the intensity $I(\tau)$ as a function of the mirror displacement $c\tau$. **b** Quantum OCT using entangled photon pairs generated in a nonlinear crystal (NLC) by the process of spontaneous parametric down-conversion and an HOM interferometer. The interferogram is a record of the photon coincidence rate $C(\tau)$ as a function of the mirror displacement $c\tau$

We have demonstrated theoretically [29,30,50,51] that Q-OCT has the following advantages in comparison with conventional OCT: (1) greater signal-to-background ratio; (2) intrinsic resolution enhancement by a factor of two for the same source bandwidth; (3) interferogram components that are insensitive to even-order dispersion of the medium; and (4) interferogram components that are sensitive to dispersion of the medium, thereby permitting direct determination of the dispersive properties of layered media.

The performance characteristics of a Q-OCT system, such as its signal-to-noise ratio (SNR) and acquisition speed, are determined by a number of factors, including the optical power (entangled-photon flux) in the interferometer [55]. We have established an approach for determining the statistical accuracy of quantum imaging in general, and the accuracy of Q-OCT in particular [44].

3.2 Q-OCT experiments

Our initial experiments demonstrated the viability of the Q-OCT technique and verified its dispersion-cancelling property [50,51] by making use of entangled photons generated by spontaneous parametric down-conversion in an 8-mm-thick lithium iodate Type-I nonlinear optical crystal pumped by a Kr^+-ion laser operated at 406 nm. As shown in Fig. 2, the experimental results confirm the theory, as described above.
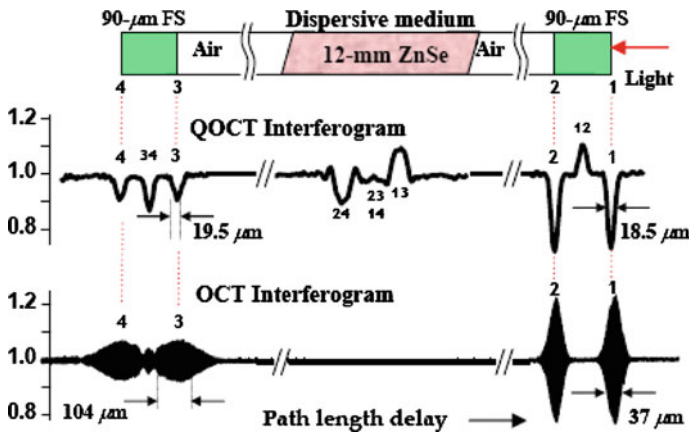

Fig. 2 Measured quantum (Q-OCT) and classical (OCT) interferograms (as a function of path-length delay) for a four-boundary sample comprising two 90-μm-thick windows of fused silica (FS) in air, with a 12-mm-thick slab of highly dispersive zinc selenide (ZnSe) between them. The light enters from the right. In classical OCT (*bottom trace*), the two boundaries not affected by the dispersive medium (denoted 1 and 2) yield interference fringes that extend for a coherence length (37μm). In contrast, the interference fringes associated with the two left-most surfaces (denoted 3 and 4) are broadened to 104μm by the dispersive medium through which the light has had to pass. In Q-OCT (*top trace*), the two right-most boundaries (1 and 2) provide interference fringes that extend for an entanglement length (18.5μm). The interference fringes associated with the two left-most surfaces (3 and 4) are broadened ever so slightly, to 19.5μm, demonstrating dispersion cancellation. Cross-interference features associated with reflections from each pair of boundaries leads to humps or dips at mid points of the single-boundary interference features; the pair of boundaries responsible for a particular cross-interference feature is designated by a pair of numbers adjacent to that feature. (After [51])
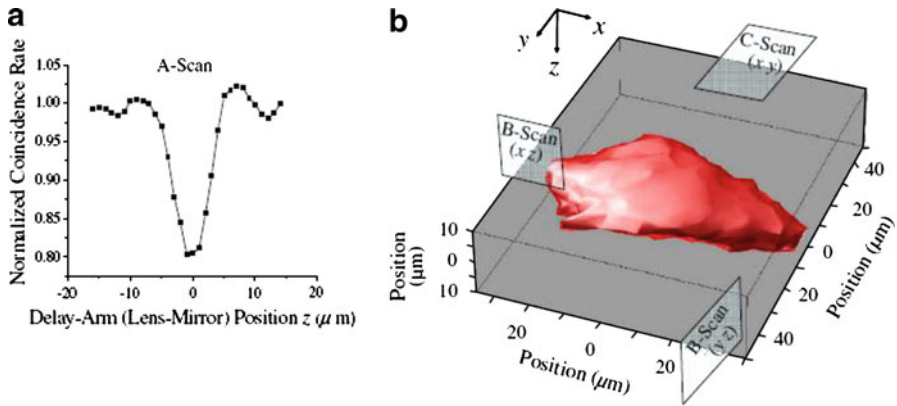
Fig. 3 **a** An A-scan showing the HOM coincidence dip that results from reflection from the top surface of an onion-skin sample coated with bovine-serum-albumin-functionalized gold nanoparticles. **b** A three-dimensional image of the biological sample at a constant normalized coincidence rate $Cx,y = 0.90$ constructed from the collection of all A-Scans. Two-dimensional sections along the orientations of the three planes indicated have been constructed. (After [55])

Our earliest Q-OCT system was limited by sub-optimal axial resolution (approximately 18.5μm), a low flux of photon pairs, and long acquisition times. A comprehensive redesign of the optical arrangement to compress all distances and miniaturize the system resulted in an increase in the photon flux by a factor of four, an enhancement of the spatial resolution by a factor of two, and an improvement in the axial resolution to 3.5μm. Moreover, Q-OCT was initially demonstrated by using a plane-wave probe beam to conduct single axial scans on simple planar samples with parallel layers of non-scattering material, in the spirit of OCDR. Incorporating scanning in the transverse direction required the use of a focused object beam, which was achieved by using a lens. Maintaining indistinguishability, and the concomitant integrity of the narrow interference dip [32], required the judicious placement of lenses in the reference beam as well.

These modifications ultimately permitted us to obtain a three-dimensional (3D) Q-OCT image of a biological specimen: an onion-skin tissue coated with functionalized gold nanoparticles [55]. The 3D image displayed in Fig. 3b, which was obtained at a constant normalized coincidence rate $C_{x,y} = 0.90$, was constructed from the collection of all axial scans (A-Scans) collected from the specimen, such as the one illustrated in Fig. 3a. The 3D images were also cast in the form of two-dimensional sections, along the orientations of the planes indicated in Fig. 3b, yielding B-Scans and C-Scans [55].

In the context of quantum information, this represents the first experiment in which a quantum-entangled entity has interacted with a biological specimen, generating a collection of quantum interferograms from which an image was constructed.

3.3 Q-OCT resolution enhancement by use of ultra-broadband entangled photons generated via chirped quasi-phase-matched SPDC

The SPDC entangled-photon flux generated in bulk nonlinear optical crystals, such as lithium iodate ($LiIO_3$) or β-barium borate (BBO), is limited [56]. The photon
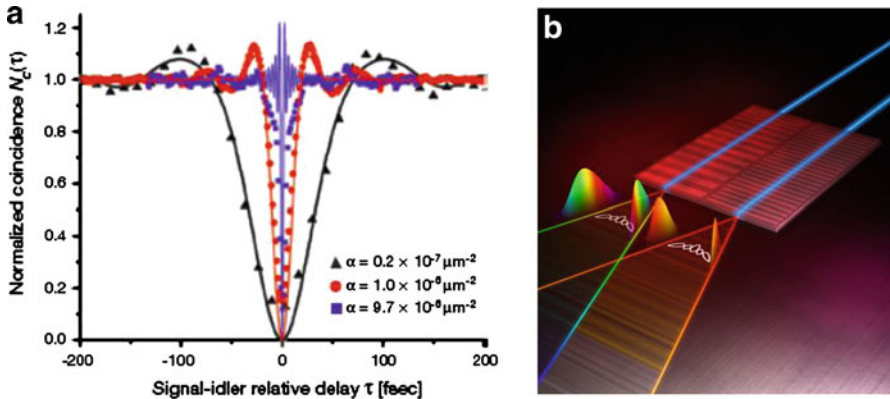
Fig. 4 **a** Normalized HOM coincidence interferograms (*dips*) for various degrees of linear chirp (indicated by the chirp parameter α) in the chirped, periodically poled, stoichiometric lithium tantalate grating. Symbols represent measured data points whereas solid curves are numerical simulations. The FWHM of the measured dips are 77, 19.1, and 7.1 fsec for the three increasing values of α, respectively. **b** Artist's rendering of the linearly chirped, periodically poled, grating used to generate the ultra-broadband entangled photons that give rise to the results shown in (**a**) (adapted from [62], magazine cover)

flux can be enhanced, however, by moving to quasi-phase-matched materials, such as periodically-poled lithium niobate ($LiNbO_3$, PPLN) or potassium titanyl phosphate ($KTiOPO_4$, KTP), which offer larger nonlinear coefficients. Indeed, PPLN waveguide structures were first suggested for producing SPDC in 2001 [57], and the conditions required to generate counterpropagating entangled photons from an unguided pump field were established shortly thereafter [58]. The generation of non-collinear and non-degenerate polarization-entangled photons via concurrent Type-I parametric down-conversion was also demonstrated in a PPLN crystal [59].

One way of generating a high flux of entangled photons that are concomitantly ultra-broadband is to make use of a quasi-phase matched nonlinear grating with a nonuniform poling period [60]. The poling pattern $\Lambda(z)$, where z is the spatial coordinate along the direction of pump propagation, provides a collection of phase matching conditions over the length of the grating, which leads to broadband biphoton generation; at the same time, the poling pattern can be chosen to engender a special phase relation among the various spectral components that will allow the biphoton wavepacket to be compressed using the techniques of ultrafast optics.

We recently made use of a Kr^+-ion cw laser pump operated at 406 nm, together with a linearly chirped, periodically poled, stoichiometric lithium tantalate grating, to generate ultra-broadband ($\sim$300 nm bandwidth) photons [61,62]. As shown in Fig. 4a, these entangled photons yielded an ultranarrow HOM dip [32], with a full-width at half-maximum (FWHM) of 7.1 fsec, corresponding to an axial resolution of 1.1 μm in Q-OCT. As indicated above, pulse-compression techniques could be used to further compress the biphoton wave function. The generation of such ultra-broadband nonclassical light opens the door to the production of a high flux of nonoverlapping entangled-photon pairs with optical powers on the order of microwatts, which could lead to the implementation of other novel quantum sensing and imaging applications,

such as entangled-photon microscopy [39], spectroscopy [63], and photoemission [64,65].

In the future, compact photonic circuits with multiple components integrated on a single chip are likely to be important for the efficient implementation of quantum photonic technologies such as Q-OCT. The possibility of using SPDC in two-mode planar and circular waveguides to generate guided-wave entangled photon pairs has been considered [66]. If the photons are confined in this manner, the spatial variables are naturally binarized and can be used to represent a modal qubit [67]. We recently considered the design of photonic circuits, based on Ti:LiNbO$_3$ diffused channel waveguides, that generate photon pairs endowed with various combinations of modal, spectral, and polarization entanglement [68]. Single- and multi-mode KTP waveguide structures have also been extensively studied for producing pulsed SPDC [69]. The principles of guided-wave SPDC are expected to be useful both for increasing the photon flux of the SPDC source and for miniaturizing the apparatus.

3.4 Q-OCT resolution enhancement by use of SSPD detectors

The silicon single-photon avalanche photodiodes (APDs) that have been used in the majority of our experiments (EG&G-SPCM-AQR-15) have limited bandwidth, particularly in the near-infrared. It follows that an even narrower HOM dip would be expected were we to use broader-bandwidth detection devices. We carried out such experiments by making use of superconducting single-photon detectors (SSPDs) [70]. These detectors were used in an HOM interferometer and the coincidence rate $N_c(\tau)$ of the detector output pulses were recorded as a function of the temporal delay τ between the signal and idler photons. These results were compared with those obtained for the silicon APDs. As displayed in Fig. 5, the HOM dip obtained using the APD
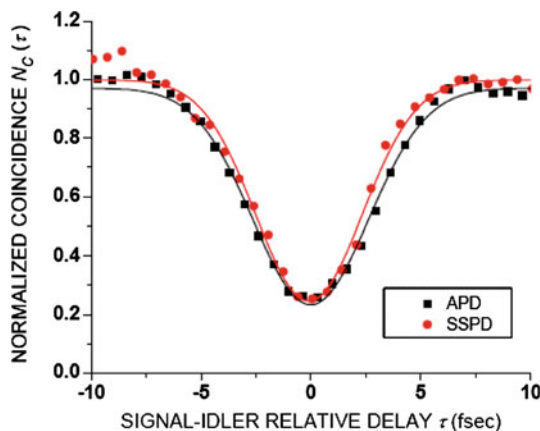

Fig. 5 Normalized HOM coincidence interferograms (*dips*) obtained using a pair of silicon single-photon APDs (*squares*), and a pair of superconducting single-photon detectors (SSPDs) (*circles*). The symbols represent the measured data points while the curves are Gaussian fits to the data. The FWHM of the measured dips are 6.2 ± 0.1 and 5.7 ± 0.2 fsec for the experiments conducted using the APDs and SSPDs, respectively. These observed ultra-narrow dips translate to ultra-high axial Q-OCT resolutions of 0.93 and 0.85 μm, respectively. (After [70])

detectors (black squares) displayed a FWHM of 6.2 ± 0.1 fsec while that obtained using the SSPD detectors (red circles) displayed a FWHM of 5.7 ± 0.2 fsec. The use of the SSPDs thus resulted in a 9% narrowing of the dip. We conclude that the use of SSPD detectors does indeed broaden the overall spectral response of the HOM interferometer, as evidenced by the narrowing of the HOM dip. This confirms that a higher density of nonoverlapping biphotons can, in fact, be obtained by making use of such detectors, thereby offering a concomitant improvement in Q-OCT resolution. These experiments offered an axial Q-OCT resolution of $0.85 \, \mu\text{m}$, a substantial improvement of the resolution of $18.5 \, \mu\text{m}$ attained in the earliest Q-OCT experiments.

It may also be worthy of mention in this connection that ultra-broadband photon-counting OCT has been carried out using parametric down-conversion generated in chirped periodically poled gratings in conjunction with superconducting single-photon detectors. Experiments were carried out at a center wavelength of 1064 nm, which is suitable for deep penetration of broadband optical radiation into biological tissue [71].

3.5 Q-OCT measurement of the dispersion coefficient of interstitial layers

As an added feature, Q-OCT permits a direct determination of the group-velocity dispersion (GVD) coefficients of the interstitial media between the reflecting surfaces of a sample [51]. A typical Q-OCT interferogram comprises two classes of features. Features in the first class, which can take the form of dips or humps, carry the information that is most often sought in OCT: the depth and reflectance of the layer surfaces that constitute the sample. In Q-OCT, each of these features is associated with a reflection from a single surface and is immune to GVD. Features in the second class, which can also take the form of dips or humps, arise from cross-interference between the reflection amplitudes associated with every pair of surfaces and are sensitive to the dispersion characteristics of the media between them. Measurement of the broadening of a feature associated with two consecutive surfaces directly yields the GVD coefficient of the interstitial medium lying between them [51]. Examples of these inter-boundary features are displayed in Fig. 2. In an OCT scan, in contrast, only a single class of features is observed; each feature is associated with reflection from a single surface and is subject to the cumulative dispersion of the portion of the sample lying above it. Thus, GVD information is not directly accessible via OCT; to measure the GVD of a particular buried medium in OCT, it is necessary to consecutively compute the GVD of each of the constituent layers above it.

3.6 Polarization-sensitive quantum optical coherence tomography (PS-Q-OCT) theory

Type-II polarization-sensitive quantum optical coherence tomography (PS-Q-OCT) offers optical sectioning with polarization-sensitive capabilities. A general Jones-matrix theory for analyzing PS-Q-OCT systems, along with a proposed procedure for carrying out such experiments, was set forth in 2004 [72]. It is an extension of the Type-I Q-OCT theory initially proposed in 2002 [29]. This approach provides a means for obtaining information about the optical path length between isotropic

reflecting surfaces, the relative magnitudes of the reflectances from each interface, the birefringence of the interstitial media, and the orientation of the optical axes of the sample. As with its precursor, PS-Q-OCT is immune to even-order sample dispersion and thereby permits measurements to be carried out at depths greater than those accessible via PS-OCT. As indicated earlier, quantum ellipsometry was developed as a tool for determining the polarization properties of thin films [38,73].

3.7 PS-Q-OCT proof-of-principle experiments

Several proof-of-principle experiments have been carried out to show that PS-Q-OCT provides results that accord with the theory [74]. The experimental arrangement is illustrated in Fig. 6. A frequency-doubled Ti:sapphire laser, used to generate 10-psec optical pulses at a center wavelength of 400 nm, pumps a BBO NLC oriented for Type-II, collinear, degenerate SPDC at a center wavelength of 800 nm. The pump beam is removed from the SPDC by a highly reflective mirror (HR 400) centered at the pump wavelength, in conjunction with a long-pass filter (LP 695). The vertically polarized signal photons and horizontally polarized idler photons are separated by a polarizing beam splitter (PBS) and fed to the sample and reference arms of a Mach-Zehnder interferometer, respectively. The polarization in the reference arm was set to horizontal (indicated by an encircled dot). In some experiments, a lens is inserted before the initial PBS.

The reference arm consists of a variable path-length delay comprised of a half-wave plate (HWP), a PBS, a quarter-wave plate (Q), and a translational mirror that changes
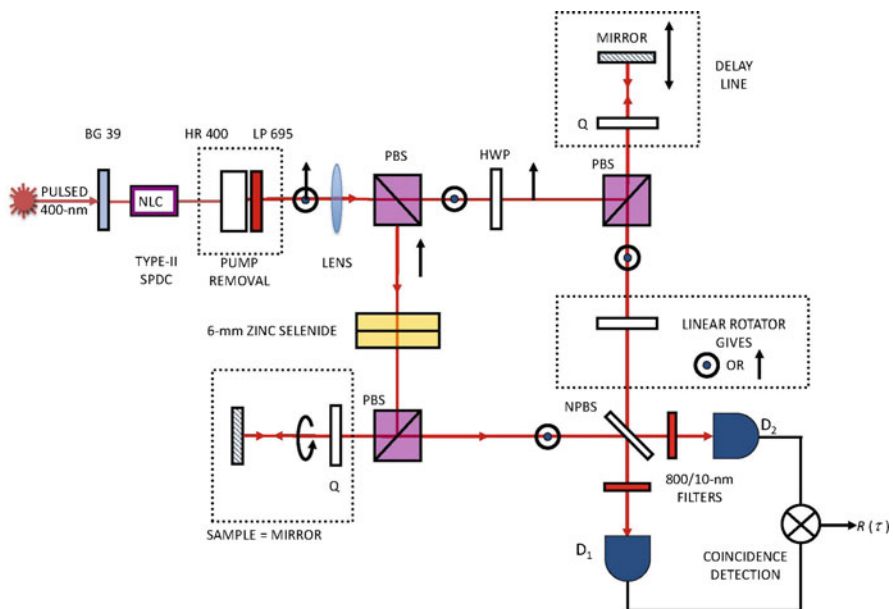

Fig. 6 Experimental arrangement used to carry out proof-of-principle polarization-sensitive quantum-optical coherence tomography (PS-Q-OCT) experiments with a ps-pulsed pump laser. (After [74])
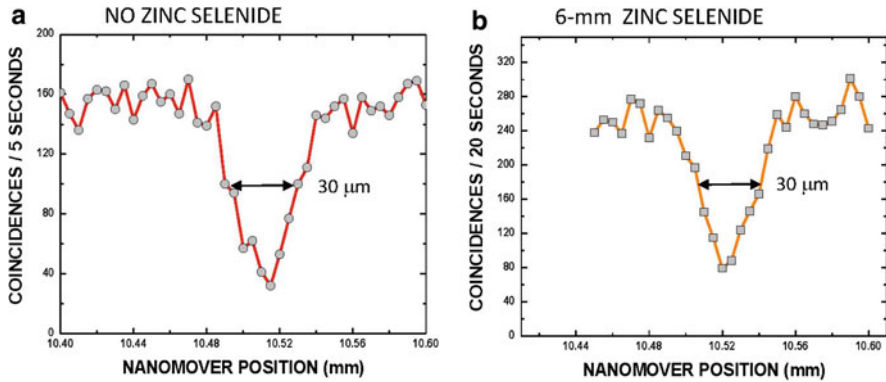
Fig. 7 Type-II Q-OCT coincidence rates $R(\tau)$ vs. path-length delay $c\tau$ with a ps-pulsed pump when the sample arm contains: **a** no ZnSe, and **b** 6 mm of dispersive ZnSe. The solid curves connect the data points to guide the eye. The measured 30-μm FWHM in (**a**) is not broadened by the presence of ZnSe in (**b**), indicating dispersion cancellation. (After [74])

the length of the reference arm relative to the sample arm. The final polarization of the reference beam can be oriented to either vertical or horizontal by a linear rotator placed before the final non-polarizing beam splitter (NPBS) of the interferometer. The sample arm contains a beam splitter, a quarter-wave plate (Q), and the sample under study; this arrangement allows circularly polarized light to impinge normally on the sample. To examine the dispersion-cancellation capabilities of PS-Q-OCT in the proof-of-principle experiments described here, we make use of a reflective mirror sample buried beneath a 6-mm thickness of ZnSe. At a wavelength of 800 nm, this material is highly dispersive; its GVD coefficient is more than 10 times greater than that of the BBO nonlinear crystal. The backscattered light from the sample travels back along the probe-beam path, through the PBS in the sample arm, to the final NPBS, where it is mixed with the delayed reference beam. In a more general configuration, the elliptically polarized backscattered light from the sample travels back along the probe-beam path through an NPBS in the sample arm, to the final NPBS. The two outputs of the final NPBS are directed through pinholes (not shown) to two single-photon-counting silicon APD detectors. The coincidence rate $R(\tau)$ for photons arriving at the two detectors, as a function of the path-length delay $c\tau$ in the reference arm, are recorded in a time window determined by a coincidence-counting detection circuit (indicated by $\otimes$).

Using the experimental arrangement portrayed in Fig. 6, with the lens removed, we carried out a set of experiments to demonstrate the cancellation of group-velocity dispersion in PS-Q-OCT. The Ti:sapphire laser was configured for psec-pulse operation, thereby generating optical pulses that are sufficiently long so that even-order dispersion cancellation is expected.

The interferograms displayed in Fig. 7 were obtained by making use of a 1.5-mm-thick BBO nonlinear crystal. Coincidence data are shown: (a) in the absence of ZnSe, and (b) with 6 mm of ZnSe placed in the sample arm before the single reflecting surface. Each data point represents the number of coincidences measured in a 5-sec

or 20-sec integration time (as indicated in Fig. 7a, b, respectively), as the path-length delay between the sample and reference arms was scanned via the translational mirror in the reference arm.

As the optical path-length delay approaches zero in Fig. 7a (at nanomover position $\sim$10.52mm), quantum destructive interference at the final beam splitter causes the observed coincidence rate to decrease, and the result is a sharp dip in the $R(\tau)$ curve. This is the HOM interference dip [32]. The interferogram in Fig. 7b behaves similarly. Indeed, the 30-μm FWHM of the dip displayed in Fig. 7b, in the presence of 6 mm of ZnSe, is the same as that shown in Fig. 7a in the absence of the ZnSe. This reveals that the presence of highly dispersive ZnSe has no effect on the width of the dip, thereby demonstrating the cancellation of group-velocity dispersion for ps-pulsed pumping in PS-Q-OCT.

Other PS-Q-OCT proof-of principle experiments have also been conducted. Pump pulses of fsec duration were used to illustrate the persistence of group-velocity dispersion when the pump pulses are of insufficient duration; the technique was successfully demonstrated for scattering samples and for lateral imaging (the lens was left in place in the setup shown in Fig. 6); and PS-Q-OCT was carried out for samples comprising two surfaces and an interstitial medium, demonstrating that PS-Q-OCT, like Q-OCT, can be used to determine the GVD coefficients of interstitial media [74].

3.8 OCT resolution enhancement by manipulation of the pump spatial distribution

An unexpected adjunct to the development of Q-OCT has been the recognition that SPDC also provides a suitable broadband source for conventional time-domain OCT under appropriate circumstances. We have shown, both theoretically and experimentally, that the spectral distribution of the signal or the idler beams in non-collinear parametric down-conversion can be controlled by changing the spatial distribution of the pump beam, via an almost one-to-one mapping. A pump beam with a small diameter generates downconverted light with a spectral distribution that is sufficiently broad (greater than 200 nm in wavelength) that sub-μm-resolution OCT can be achieved. Indeed, OCT interferograms from a 2-μm thick pellicle confirmed the efficacy of this approach [75,76]. We also demonstrated experimentally that a similar approach permits the generation of entangled photon pairs with a broad joint spectrum. Such spectral properties are mediated by the geometry of non-collinear spontaneous parametric down-conversion and by selecting the appropriate spatial profile of the pump laser light. The width of both (i) the joint spectrum of the entangled photon pairs, and (ii) the spectrum of the individual signal and idler photons, can be tailored over a large range of values, which renders this technique of potential value for quantum-information applications. We have reported experimental results that demonstrate an OCT axial resolution $\sim$1μm [76,77].

3.9 Algorithms for OCT and Q-OCT image reconstruction

We have explored the possibility of extending the notion of compressed sensing (CS) to spectral-domain OCT, potentially allowing the use of detector arrays of decreased size [78]. CS techniques can yield accurate signal reconstructions from highly

undersampled measurements, i.e., data that is sampled significantly below the Nyquist rate. The Fourier relationship between the measurements and the desired signal in spectral-domain OCT makes it a good candidate for compressed sensing. Fourier measurements represent good linear projections for the compressed sensing of sparse point-like signals by random under-sampling of frequency-domain data, and axial scans in OCT are generally sparse in nature. This property has recently been used to reduce speckle in OCT images. We have carried out simulations to demonstrate the usefulness of CS for simplifying detection schemes in spectral-domain OCT. In particular, we have demonstrated the reconstruction of a sparse axial scan by using fewer than 10 percent of the measurements required by standard spectral-domain OCT.

Research on data processing to extract axial images from Q-OCT interferograms has also been carried out by formulating the problem for the special case of layered samples. We have examined new algorithms for solving this problem, even when there are a large number of interacting layers, using least-square-error estimation techniques [79]. The program estimates the positions and reflectances of the layers. This problem offers continuing challenges, however, particularly when the layers are not well separated.

4 Origin and development of quantum-mimetic optical coherence tomography

4.1 Phase-conjugate optical coherence tomography (PC-OCT) theory

The successful demonstration of Q-OCT has spurred interest in methods that utilize classical light to mimic the quantum technique and reap the same principal advantages, namely even-order dispersion cancellation and an axial resolution enhancement of a factor of two. In Q-OCT, SPDC generates signal and reference beams with a nonclassical phase-sensitive cross correlation, and two-photon coincidence detection, which is a fourth-order interference phenomenon, is used for measurement [29]. The key to achieving the resolution improvement and dispersion cancellation in Q-OCT can thus be understood in terms of a phase-sensitive cross correlation engendered by quantum entanglement, while the low-flux SPDC provides a measurement advantage with nearly background-free coincidence detection. It turns out, however, that classical light can also possess a phase-sensitive cross correlation. In phase-conjugate OCT (PC-OCT), classical signal and reference beams with phase-sensitive cross correlation are used in a double-pass configuration to achieve a factor-of-two resolution enhancement, as portrayed in Fig. 8; phase conjugation provides the means for cancelling even-order dispersion [45]. Moreover, the phase conjugation converts the phase-sensitive cross correlation into a phase-insensitive cross correlation that can be detected in second-order interference, as used in standard interferometry, rather than in fourth-order interference as required for Q-OCT. Signal-to-noise ratios are found to be comparable for Q-OCT and PC-OCT, thereby making PC-OCT a classical alternative for potential applications.
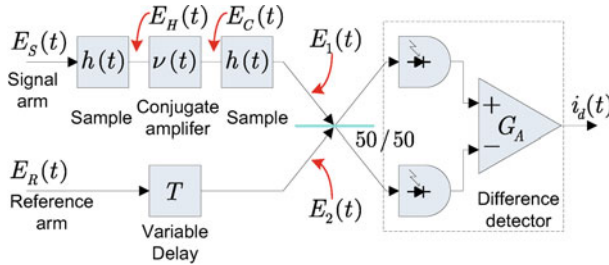
Fig. 8 Schematic of phase-conjugate OCT using classical signal and reference light with phase-sensitive cross correlation. The sample is interrogated twice in a double-pass configuration and the amplifier provides signal amplification and phase conjugation to achieve dispersion cancellation. (After [45])
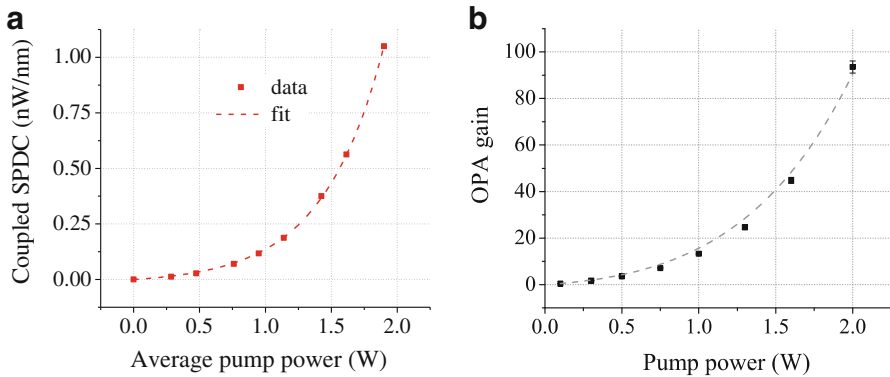

Fig. 9 **a** Plot of fiber-coupled SPDC output at 1560 nm as a function of average pump power, showing amplification of spontaneous emission. At an input power of 2 W, the output pulses contained 600 photons with a 5-nm bandwidth. **b** Plot of the optical parametric amplifier gain as a function of pump power; a gain of nearly 20 dB is achieved at 2 W input. (After [46])

4.2 Pulsed SPDC source for PC-OCT

While SPDC is the standard method for generating entangled photon pairs, at high flux levels it is also an ideal classical light source of phase-sensitive cross-correlated signal and reference beams. We employed pulsed SPDC to create signal and reference pulses that contained hundreds of photons per pulse [46]. With mean photon numbers far higher than unity, these pulses behave classically and no entanglement exists between the signal and reference pulses. With an average power of 2 W and peak powers at the kW level, we observed amplified SPDC in PPLN, as evidenced by the exponential increase of the output power at high pump powers in Fig. 9a. The pulsed SPDC was also broadband, with a measured bandwidth of 143 nm. Figure 9b displays the PPLN-based optical parametric amplifier reaching a single-pass gain of nearly 20 dB; this was used as the phase conjugator and amplifier in our PC-OCT proof-of-principle experiment.
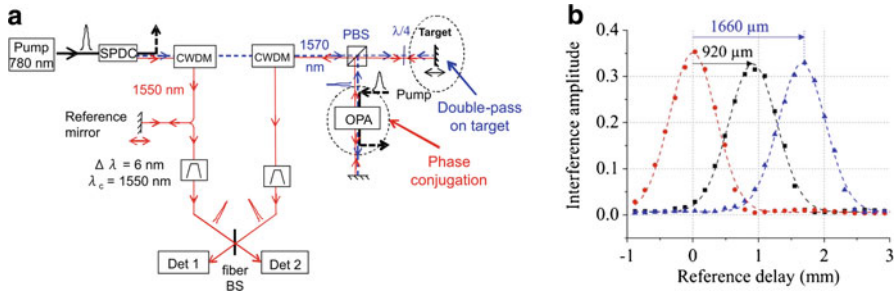
Fig. 10 a PC-OCT experimental setup. A coarse wavelength division multiplexer (CWDM) separates the SPDC output into 1570-nm signal and 1550-nm reference beams. The conjugate signal at 1550 nm that emerges from the OPA interrogates the target a second time before making conjugate signal-reference interferometric measurements. **b** PC-OCT interferograms at three different target positions. Reference delays were twice as large as would be expected from mirror-position shifts, thereby indicating a factor-of-two resolution enhancement. The envelope width was measured to be ∼0.89 mm; it would have been 3.02 mm without dispersion cancellation. (After [47])

4.3 PC-OCT proof-of-principle experiment

We demonstrated the PC-OCT concept in a tabletop proof-of-principle experiment [47]. Instead of imaging a biological sample, we measured the longitudinal resolution enhancement of the position of a movable mirror in a laser-radar setting. As a first demonstration, we utilized only a small portion (∼6 nm) of the available 143-nm bandwidth, and we deliberately introduced dispersion into the measurement by propagating the short pulses (< 1 ps) through a substantial length of optical fiber. In the experimental arrangement shown in Fig. 10a, the signal light that was reflected from the target was phase conjugated and amplified, and the conjugate signal was sent to the target a second time. The reflected conjugate signal was then mixed with the time-delayed reference light to yield the interferograms of Fig. 10b. The conjugate signal and reference beams had an average power of 2.5 nW so that a standard InGaAs detector was suitable for making the measurement. We showed that there was indeed a factor of two improvement in the axial resolution and that the dispersion in the signal arm was completely cancelled. While atmospheric dispersion is minimal at optical wavelengths, the technique can be applied equally well to microwave wavelengths where such dispersion is more severe. This is a good first step toward applying the PC-OCT technique to biological samples where dispersion is significant and a much broader bandwidth from a chirped PPLN crystal [61,62] is needed to obtain adequate resolution.

4.4 Chirped-pulse OCT (CP-OCT) experiment

PC-OCT is not the only quantum-mimetic technique that can achieve the measurement advantages of Q-OCT while using classical light. Resch and coworkers recognized that biphotons generated under SPDC are anticorrelated in their frequencies such that their sum is always equal to the narrowband pump frequency. This frequency anticorrelation property can be reproduced in classical frequency-chirped pulses with one pulse that is positively chirped, $\omega_0 + \Omega$, while the other is negatively chirped,
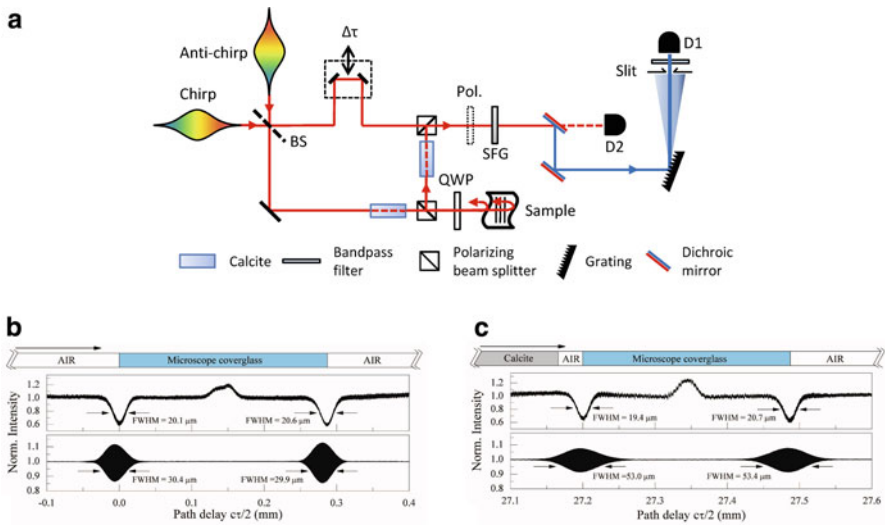
Fig. 11 **a** Schematic of the experimental arrangement for CP-OCT. Interferogram measurements are carried out using narrowband SFG. **b** CP-OCT interferogram (*top*) versus white-light interferogram (*bottom*), in the absence of dispersion, showing a resolution enhancement of $\sqrt{2}$. **c** CP-OCT interferogram (*top*) versus white-light interferogram (*bottom*), in the presence of dispersion introduced by a piece of calcite placed in front of the microscope cover-glass sample, demonstrating dispersion cancellation. (After [49])

$\omega_0 - \Omega$, where ω_0 is the average frequency. So-called chirped-pulse interfereometry can reproduce many of the interferometric features that have been demonstrated using biphotons [48]. In chirped-pulse OCT, oppositely chirped pulses are fed to an interferometer, as shown in Fig. 11a. One arm of the interferometer contains the sample and the two pulses are combined at its output. Detection is via sum-frequency generation (SFG) in a nonlinear optical crystal and narrowband filtering is used to extract the $2\omega_0$ component, thereby ensuring that the output is restricted to cross-correlations between the oppositely chirped pulses [49]. Figure 11b displays a resolution enhancement of $\sqrt{2}$ for chirped-pulse OCT in comparison with white-light interferometry, in the absence of dispersion, which is not quite as good as the factor of 2 improvement obtained for both Q-OCT and PC-OCT. Dispersion cancellation has also been demonstrated in CP-OCT by inserting a piece of calcite in front of the microscope cover-glass sample to simulate dispersion, as shown in Fig. 11c. CP-OCT has the advantage that bright chirped and anti-chirped pulses are readily generated so that the output signal-to-noise ratio can be far higher, and the acquisition rate far greater, than is possible with Q-OCT. It is clear from these, as well as other experiments [80], that entanglement is not a prerequisite for achieving dispersion cancellation.

5 Conclusion

We have demonstrated axial Q-OCT imaging for multi-layered and scattering media. Dispersion cancellation has been demonstrated experimentally. In conjunction with this, a method for measuring the dispersion coefficient of the interstitial media between

boundaries in the sample has been developed and validated. Resolution enhancement in the transverse direction has been concomitantly achieved with improved resolution in the axial direction by making the Q-OCT apparatus compact and by judiciously inserting optical elements that leave path indistinguishability in place to insure robust interference patterns. Three-dimensional images of a biological sample have been obtained in the form of A-, B-, and C-scans. A statistical analysis of Q-OCT measurement accuracy has been carried out.

Novel periodically-poled, and chirped quasi-phase-matched (chirped-QPM), nonlinear-optical structures have been conceived, fabricated, and used to generate ultra-broadband SPDC and thereby to improve the resolution available in Q-OCT, as well as in OCT. Q-OCT resolution has been further enhanced, to a value of 0.85μm, by the use of superconducting single-photon detectors (SSPDs). It has been shown that OCT resolution can be enhanced by manipulating the pump spatial distribution. A polarization-sensitive version of Q-OCT, known as PS-Q-OCT, has been analyzed and constructed, and its behavior has been shown to be in accord with theoretical predictions.

The use of chirped-QPM SPDC and SSPDs have also been shown to improve the resolution of photon-counting OCT centered at a wavelength of 1064 nm, which is suitable for achieving deep penetration of broadband optical radiation into biological tissue. Attention has been drawn to the principles of guided-wave SPDC, which can be used to increase photon flux and miniaturize the apparatus. Two data processing tools have been briefly examined: algorithms for image reconstruction in Q-OCT and compressed sensing in spectral-domain OCT.

Quantum-mimetic optical coherence tomography (QM-OCT), in the form of phase-conjugate optical coherence tomography (PC-OCT) and chirped-pulse optical coherence tomography (CP-OCT), have been shown to successfully mimic dispersion cancellation and other salutary features of Q-OCT. These implementations have the advantage that they make use of classical, rather than nonclassical, light. Various versions of QM-OCT also offer unique additional benefits, such as enhanced signal-to-noise ratio and acquisition rate.

References

1. Youngquist, R.C., Carr, S., Davies, D.E.N.: Optical coherence-domain reflectometry: a new optical evaluation technique. Opt. Lett. **12**, 158–160 (1987)
2. Takada, K., Yokohama, I., Chida, K., Noda, J.: New measurement system for fault location in optical waveguide devices based on an interferometric technique. Appl. Opt. **26**, 1603–1606 (1987)
3. Danielson, B.L., Whittenberg, C.D.: Guided-wave reflectometry with micrometer resolution. Appl. Opt. **26**, 2836–2842 (1987)
4. Gilgen, H.H., Novàk, R.P., Salathé, R.P., Hodel, W., Beaud, P.: Submillimeter optical reflectometry. J. Lightwave Technol. **7**, 1225–1233 (1989)
5. Huang, H., Swanson, E.A., Lin, C.P., Schuman, J.S., Stinson, W.G., Chang, W., Hee, M.R., Flotte, T., Gregory, K., Puliafito, C.A., Fujimoto, J.G.: Optical coherence tomography. Science **254**, 1178–1181 (1991)

6. Fercher, A.F., Hitzenberger, C.K.: Optical coherence tomography. In: Wolf , E. (ed.) Progress in Optics, vol. 44, chap 4., pp. 215–302. Elsevier, Amsterdam (2002)

7. Tomlins, P.H., Wang, R.K.: Theory, developments and applications of optical coherence tomography. J. Phys. D: Appl. Phys. **38**, 2519–2535 (2005)

8. Brezinski, M.E.: Optical Coherence Tomography: Principles and Applications. Academic, San Diego (2006)

9. Zysk, A.M., Nguyen, F.T., Oldenburg, A.L., Marks, D.L., Boppart, S.A.: Optical coherence tomography: A review of clinical development from bench to bedside. J. Biomed. Opt. **12**, 051403 (2007)

10. Drexler, W., Fujimoto, J. (eds.): Optical Coherence Tomography: Technology and Applications. Springer, Berlin (2008)

11. Saleh, B.E.A.: Introduction to Subsurface Imaging, chaps 3 and 4. Cambridge University Press, Cambridge (2011)

12. Eigenwillig, C.M., Biedermann, B.R., Wieser, W., Huber, R.: Wavelength swept amplified spontaneous emission source. Opt. Express **17**, 18794–18807 (2009)

13. Teich, M.C., Keyes, R.J., Kingston, R.H.: Optimum heterodyne detection at $10.6\,\mu\mathrm{m}$ in photoconductive Ge:Cu. Appl. Phys. Lett. **9**, 357–360 (1966)

14. Teich, M.C.: Laser heterodyning. J. Mod. Opt. (Optica Acta) **32**, 1015–1021 (1985)

15. Hitzenberger, C.K., Baumgartner, A., Drexler, W., Fercher, A.F.: Dispersion effects in partial coherence interferometry: Implications for intraocular ranging. J. Biomed. Opt. **4**, 144–151 (1999)

16. Drexler, W., Morgner, U., Ghanta, R.K., Kärtner, F.X., Schuman, J.S., Fujimoto, J.G.: Ultrahigh-resolution ophthalmic optical coherence tomography. Nat. Med. **7**, 502–507 (2001)

17. Fercher, A.F., Hitzenberger, C.K., Sticker, M., Zawadzki, R., Karamata, B., Lasser, T.: Dispersion compensation for optical coherence tomography depth-scan signals by a numerical technique. Opt. Commun. **204**, 67–74 (2002)

18. Smith, E.D.J., Zvyagin, A.V., Sampson, D.D.: Real-time dispersion compensation in scanning interferometry. Opt. Lett. **27**, 1998–2000 (2002)

19. Fercher, A.F., Hitzenberger, C.K., Sticker, M., Zawadzki, R., Karamata, B., Lasser, T.: Numerical dispersion compensation for partial coherence interferometry and optical coherence tomography. Opt. Express **9**, 610–615 (2001)

20. Teich, M.C., Saleh, B.E.A., Stoler, D.: Antibunching in the Franck-Hertz experiment. Opt. Commun. **46**, 244–248 (1983)

21. Teich, M.C., Saleh, B.E.A.: Observation of sub-Poisson Franck-Hertz light at 253.7 nm. J. Opt. Soc. Am. B **2**, 275–282 (1985)

22. Teich, M.C., Saleh, B.E.A.: Photon bunching and antibunching. In: Wolf, E. (ed.) Progress in Optics, vol. 26, chap 1., pp. 1–104. North-Holland/Elsevier, Amsterdam (1988)

23. Teich, M.C., Saleh, B.E.A.: Squeezed states of light. Quantum Opt. **1**, 153–191 (1989) [Reprinted in Tutorials in Optics, Moore, D.T. (ed.) Optical Society of America, Washington, D.C. (1992), chap. 3, pp. 29–52]

24. Teich, M.C., Saleh, B.E.A.: Squeezed and antibunched light. Phys. Today **43**(6), 26–34 (1990)

25. Peřina, J., Hradil, Z., Jurčo, B.: Quantum Optics and Fundamentals of Physics. chaps. 7 and 8. Kluwer, Boston (1994)

26. Mandel, L., Wolf, E.: Optical Coherence and Quantum Optics. Chap 22. Cambridge University Press, New York (1995)

27. Klyshko, D.N.: Photons and Nonlinear Optics. Nauka, Moscow (1980), chaps. 1 and 6 [Translation: Gordon and Breach, New York (1988)]

28. Saleh, B.E.A., Teich, M.C.: Fundamentals of Photonics 2nd edn. Wiley, Hoboken (2007)

29. Abouraddy, A.F., Nasr, M.B., Saleh, B.E.A., Sergienko, A.V., Teich, M.C.: Quantum-optical coherence tomography with dispersion cancellation. Phys. Rev. A **65**, 053817 (2002)

30. Teich, M.C., Saleh, B.E.A., Sergienko, A.V., Abouraddy, A.F., Nasr, M.B.: Quantum Optical Coherence Tomography Data Collection Apparatus and Method for Processing Therefor. U.S. Patent Number 6,882,431, issued 19 April 2005, 6 claims

31. Teich, M.C., Wolga, G.J.: Multiple-photon processes and higher order correlation functions. Phys. Rev. Lett. **16**, 625–628 (1966)

32. Hong, C.K., Ou, Z.Y., Mandel, L.: Measurement of subpicosecond time intervals between two photons by interference. Phys. Rev. Lett. **59**, 2044–2046 (1987)

33. Larchuk, T., Campos, R.A., Rarity, J.G., Tapster, P.R., Jakeman, E., Saleh, B.E.A., Teich, M.C.: Interfering entangled photons of different colors. Phys. Rev. Lett. **70**, 1603–1606 (1993)

34. Fei, H.-B., Jost, B.M., Popescu, S., Saleh, B.E.A., Teich, M.C.: Entanglement-induced two-photon transparency. Phys. Rev. Lett. **78**, 1679–1682 (1997)
35. Yarnall, T., Abouraddy, A.F., Saleh, B.E.A., Teich, M.C.: Spatial coherence effects in second- and fourth-order temporal interference. Opt. Express **16**, 7634–7640 (2008)
36. Walton, Z.D., Abouraddy, A.F., Sergienko, A.V., Saleh, B.E.A., Teich, M.C.: Decoherence-free sub-spaces in quantum key distribution. Phys. Rev. Lett. **91**, 087901 (2003)
37. Hayat, M., Abdullah, S., Joobeur, A., Saleh, B.: Maximum likelihood image estimation using photon-correlated beams. IEEE Trans. Image Proc. **11**, 838–846 (2002)
38. Toussaint, K.C. Jr., Di Giuseppe, G., Bycenski, K.J., Sergienko, A.V., Saleh, B.E.A., Teich, M.C.: Quantum ellipsometry using correlated-photon beams. Phys. Rev. A **70**, 023801 (2004)
39. Teich, M.C., Saleh, B.E.A.: Mikroskopie s kvantově provázanými fotony (in Czech), Československý časopis pro fyziku **47**, 3–8 (1997) [Translation: Entangled-photon microscopy. http://people.bu.edu/teich/pdfs/Cesk-English-47-3-1997.pdf]; U.S. Patent No. 5,796,477 (1998)
40. Abouraddy, A.F., Saleh, B.E.A., Sergienko, A.V., Teich, M.C.: Role of entanglement in two-photon imaging. Phys. Rev. Lett. **87**, 123602 (2001)
41. Abouraddy, A.F., Saleh, B.E.A., Sergienko, A.V., Teich, M.C.: Quantum holography. Opt. Express **9**, 498–505 (2001)
42. Saleh, B.E.A., Abouraddy, A.F., Sergienko, A.V., Teich, M.C.: Duality between partial coherence and partial entanglement. Phys. Rev. A **62**, 043816 (2000)
43. Abouraddy, A.F., Saleh, B.E.A., Sergienko, A.V., Teich, M.C.: Entangled-photon Fourier optics. J. Opt. Soc. Am. B **19**, 1174–1184 (2002)
44. Saleh, B.E.A, Teich, M.C.: Noise in classical and quantum photon-correlation imaging. In: Friberg, A.T., Dändliker, R. (eds.) Advances in Information Optics and Photonics, vol. **PM183**, SPIE Press, Bellingham, WA (2008), chap. 21, pp. 423–435
45. Erkmen, B.I., Shapiro, J.H.: Phase-conjugate optical coherence tomography. Phys. Rev. A **74**, 041601(R) (2006)
46. Le Gouët, J., Venkatraman, D., Wong, F.N.C., Shapiro, J.H.: Classical low-coherence interferometry based on broadband parametric fluorescence and amplification. Opt. Express **17**, 17874–17887 (2009)
47. Le Gouët, J., Venkatraman, D., Wong, F.N.C., Shapiro, J.H.: Experimental realization of phase-con-jugate optical coherence tomography. Opt. Lett. **35**, 1001–1003 (2010)
48. Kaltenbaek, R., Lavoie, J., Resch, K.J.: Classical analogues of two-photon quantum interference. Phys. Rev. Lett. **102**, 243601 (2009)
49. Lavoie, J., Kaltenbaek, R., Resch, K.J.: Quantum-optical coherence tomography with classical light. Opt. Express **17**, 3818–3825 (2009)
50. Nasr, M.B., Saleh, B.E.A., Sergienko, A.V., Teich, M.C.: Demonstration of dispersion-cancelled quan-tum-optical coherence tomography. Phys. Rev. Lett. **91**, 083601 (2003)
51. Nasr, M.B., Saleh, B.E.A., Sergienko, A.V., Teich, M.C.: Dispersion-cancelled and dispersion-sensitive quantum optical coherence tomography. Opt. Express **12**, 1353–1362 (2004)
52. Steinberg, A.M., Kwiat, P.G., Chiao, R.Y.: Dispersion cancellation and high-resolution time measure-ments in a fourth-order optical interferometer. Phys. Rev. A **45**, 6659–6665 (1992)
53. Larchuk, T.S., Teich, M.C., Saleh, B.E.A.: Nonlocal cancellation of dispersive broadening in Mach-Zehnder interferometers. Phys. Rev. A **52**, 4145–4154 (1995)
54. Minaeva, O., Bonato, C., Saleh, B.E.A., Simon, D.S., Sergienko, A.V.: Odd- and even-order dispersion cancellation in quantum interferometry. Phys. Rev. Lett. **102**, 100504 (2009)
55. Nasr, M.B., Goode, D.P., Nguyen, N., Rong, G., Yang, L., Reinhard, B.M., Saleh, B.E.A., Teich, M.C.: Quantum optical coherence tomography of a biological sample. Opt. Commun. **282**, 1154–1159 (2009)
56. Nasr, M.B., Di Giuseppe, G., Saleh, B.E.A., Sergienko, A.V., Teich, M.C.: Generation of high-flux ultra-broadband light by bandwidth amplification in spontaneous parametric down-conversion. Opt. Commun. **246**, 521–528 (2005)
57. Tanzilli, S., De Riedmatten, H., Tittel, W., Zbinden, H., Baldi, P., De Micheli, M., Ostrowsky, D.B., Gisin, N.: Highly efficient photon-pair source using periodically poled lithium niobate waveguide. Elec-tron. Lett. **37**, 26–28 (2001)
58. Booth, M.C., Atatüre, M., Di Giuseppe, G., Saleh, B.E.A., Sergienko, A.V., Teich, M.C.: Counterpropa-gating entangled photons from a waveguide with periodic nonlinearity. Phys. Rev. A **66**, 023815 (2002)

59. Guillet de Chatellus, H., Sergienko, A.V., Saleh, B.E.A., Teich, M.C., Di Giuseppe, G.: Non-collinear and non-degenerate polarization-entangled photon generation via concurrent type-I parametric downconversion in PPLN. Opt. Express **14**, 10060–10072 (2006)
60. Carrasco, S., Torres, J.P., Torner, L., Sergienko, A.V., Saleh, B.E.A., Teich, M.C.: Enhancing the axial resolution of quantum optical coherence tomography by aperiodic quasi-phase-matching. Opt. Lett. **29**, 2429–2431 (2004)
61. Nasr, M.B., Carrasco, S., Saleh, B.E.A., Sergienko, A.V., Teich, M.C., Torres, J.P., Torner, L., Hum, D.S., Fejer, M.M.: Ultrabroadband biphotons generated via chirped quasi-phase-matched optical parametric down-conversion. Phys. Rev. Lett. **100**, 183601 (2008)
62. Teich, M.C., Nasr, M.B., Carrasco, S., Saleh, B.E.A., Sergienko, A.V., Torres, J.P., Torner, L., Hum, D.S., Fejer, M.M.: Generating ultra-broadband biphotons via chirped QPM down-conversion. Opt. Photonics News **19** (12), p. 36 and Magazine Cover (2008)
63. Saleh, B.E.A., Jost, B.M., Fei, H.-B., Teich, M.C.: Entangled-photon virtual-state spectroscopy. Phys. Rev. Lett. **80**, 3483–3486 (1998)
64. Lissandrin, F., Saleh, B.E.A., Sergienko, A.V., Teich, M.C.: Quantum theory of entangled-photon photoemission. Phys. Rev. B **69**, 165317 (2004)
65. Booth, M.C., Saleh, B.E.A., Sergienko, A.V., Teich, M.C.: Temperature and wavelength dependence of Fermi-tail photoemission and two-photon photoemission from multialkali semiconductors. J. Appl. Phys. **100**, 023521 (2006)
66. Saleh, M.F., Saleh, B.E.A., Teich, M.C.: Modal, spectral, and polarization entanglement in guided-wave parametric down-conversion. Phys. Rev. A **79**, 053842 (2009)
67. Saleh, M.F., Di Giuseppe, G., Saleh, B.E.A., Teich, M.C.: Modal and polarization qubits in Ti:LiNbO$_3$ photonic circuits for a universal quantum logic gate. Opt. Express **18**, 20475–20490 (2010)
68. Saleh, M.F., Di Giuseppe, G., Saleh, B.E.A., Teich, M.C.: Photonic circuits for generating modal, spectral, and polarization entanglement. IEEE Photonics J. **2**, 736–752 (2010)
69. Fiorentino, M., Spillane, S.M., Beausoleil, R.G., Roberts, T.D., Battle, P., Munro, MW.: Spontaneous parametric down-conversion in periodically poled KTP waveguides and bulk crystals. Opt. Express **15**, 7479–7488 (2007)
70. Nasr, M.B., Minaeva, O., Goltsman, G.N., Sergienko, A.V., Saleh, B.E.A., Teich, M.C.: Submicron axial resolution in an ultrabroadband two-photon interferometer using superconducting single-photon detectors. Opt. Express **16**, 15104–15108 (2008)
71. Mohan, N., Minaeva, O., Goltsman, G.N., Saleh, M.F., Nasr, M.B., Sergienko, A.V., Saleh, B.E.A., Teich, M.C.: Ultra-broadband coherence-domain imaging using parametric downvonversion and superconducting single-photon detectors at 1064 nm. Appl. Opt. **48**, 4009–4017 (2009)
72. Booth, M.C., Di Giuseppe, G., Saleh, B.E.A., Sergienko, A.V., Teich, M.C.: Polarization-sensitive quantum-optical coherence tomography. Phys. Rev. A **69**, 043815 (2004)
73. Abouraddy, A.F., Toussaint, K.C. Jr., Sergienko, A.V., Saleh, B.E.A., Teich, M.C.: Ellipsometric measurements using photon pairs generated by spontaneous parametric down-conversion. Opt. Lett. **26**, 1717–1719 (2001)
74. Booth, M.C., Saleh, B.E.A., Teich, M.C.: Polarization-sensitive quantum-optical coherence tomography: Experiment. Opt. Commun. **284**, 2542–2549 (2011)
75. Carrasco, S., Torres, J.P., Torner, L., Sergienko, A.V., Saleh, B.E.A., Teich, M.C.: Spatial-to-spectral mapping in spontaneous parametric downconversion. Phys. Rev. A **70**, 043817 (2004)
76. Carrasco, S., Sergienko, A.V., Saleh, B.E.A., Teich, M.C., Torres, J.P., Torner, L.: Spectral engineering of entangled two-photon states. Phys. Rev. A **73**, 063802 (2006)
77. Carrasco, S., Nasr, M.B., Sergienko, A.V., Saleh, B.E.A., Teich, M.C., Torres, J.P., Torner, L.: Broadband light generation by noncollinear parametric downconversion. Opt. Lett. **31**, 253–255 (2006)
78. Mohan, N., Stojanovic, I., Karl, W.C., Saleh, B.E.A., Teich, M.C.: Compressed sensing in optical coherence tomography. In: Conchello, J.-A., Cogswell, C. J., Wilson, T., Brown, T.G. (eds.) Proceedings of SPIE **7570** (Three-Dimensional and Multidimensional Microscopy: Image Acquisition and Processing), p. 75700L (2010)
79. Pavlovich, J., Karl, W.C., Saleh, B.E.A., Sergienko, A.V., Teich, M.C.: Parameter estimation in quantum optical coherence tomography. OSA/FIO, Paper JWA53 (2005)
80. Torres-Company, V., Valencia, A., Hendrych, M., Torres, J.P.: Cancellation of dispersion and temporal modulation with nonentangled frequency-correlated photons. Phys. Rev. A **83**, 023824 (2011)